applied sciences

MDPI

Article

Design of a Phase Calibrator to Evaluate Non-Matched Microphones for Intensity Probes

Nicola Russo [1,2,†], Ernesto Monaco [1,*,†] and Andrea Esposito [2,†]

[1] Industrial Engineering Department, University of Naples Federico II, Via Claudio 21, 80125 Napoli, Italy; russo@sonorasrl.com
[2] Sonora Srl, 81100 Caserta, Italy; esposito@sonorasrl.com
* Correspondence: ermonaco@unina.it
† These authors contributed equally to this work.

Abstract: Intensity measurements represent a well-established method to determine the sound power of an emitting object. The principal strength of this technique relies upon the possibility of performing the measurements in situ, with no special required conditions concerning the surrounding sound field. Commercially available sound intensity probes rely on two phase-matched microphones properly spaced concerning the desired frequency range. Given the physical and mathematical principles behind the intensity method, phase differences between the signals assume a crucial role. This report aims to study the possibility of designing a cost-effective acoustic phase calibrator to extract the intrinsic phase mismatch of standard class-1 microphones. A phase calibrator has been designed to identify phase mismatches between the microphones and provide the required corrections at specific frequencies. Numerical acoustical Finite Element Method (FEM). models of the calibrator configurations have been implemented. The results of the numerical models have lately led to three calibrator prototypes that have been produced by 3D-printing and tested. They have shown good results when compared to a commercially available and much more expensive acoustic coupler.

Keywords: sound intensity probe; acoustic phase calibrator; microphones; phase difference

Citation: Russo, N.; Monaco, E.; Esposito, A. Design of a Phase Calibrator to Evaluate Non-Matched Microphones for Intensity Probes. *Appl. Sci.* **2023**, *13*, 12324. https://doi.org/10.3390/app132212324

Academic Editor: Lamberto Tronchin

Received: 4 August 2023
Revised: 30 October 2023
Accepted: 3 November 2023
Published: 14 November 2023

1. Introduction

Sound intensity measurements represent a standard for determining the acoustic power that a piece of generic machinery can radiate [1–3]. Its success is based on the peculiar characteristic of not being influenced by the surrounding acoustic environment. This has been obtained, until today, by building acoustic intensity probes only by "matched" microphones guaranteeing the maximum correlation between their measurements in terms of amplitude and phase responses. This correlation is also periodically verified by very expensive calibrators, in which the two microphones are exposed contemporarily at the same acoustic fields, providing frequency response functions in which the amplitude represents the ratio of acoustic magnitudes and the difference between the two respective microphones phases (due only to intrinsic mismatch). Sound intensity probes are, therefore, complex devices that allow accurate measurements but are not always sustainable for companies or professionals. Therefore, as the first step toward the development of a more cost-effective instrument, we have designed an acoustic calibrator that can match the phases of two generic microphones not explicitly designed for intensity probes. The sound intensity is a measurement of the acoustic energy that flows through a unit area along a direction perpendicular to it. The intensity can be expressed through the product between the pressure (p) and the particle velocity component (v), as represented in Equation (1).

$$I = pv \tag{1}$$

The average sound intensity during time T is given by Equation (2):

$$< I >= \frac{1}{T}\int_0^T p(t)u(t)dt \tag{2}$$

In the case of the so-called *p-p* probes, the intensity measurement occurs by deploying two closely placed microphones, appropriately spaced concerning an imposed frequency error bound [4,5]. From a mathematical formulation, the particle velocity can be obtained with the linearized Euler equation; it is possible to assume the pressure gradient as the pressure difference on the distance between the two microphones [6–8].

$$u(t)_r = -\int_{-\infty}^{t} \frac{p(t)_2 - p(t)_1}{\Delta r \rho} \tag{3}$$

From Equation (3), in which $p_{1,2}$ is the pressure as measured by the microphones while Δr and ρ represent, respectively, the fixed distance between the microphones and the fluid density, it is evident that the particle velocity can be linked to the pressure difference between the microphones and, therefore, to the time delay between the signals. That translates into a frequency mismatch between the signals. By considering the formulation reported in [9], it is possible to compute the sound intensity by evaluating the imaginary part of the cross-spectrum $G(f)_{1,2}$, which represents the phase difference itself as a function of the frequency f. This formulation is reliable if it is possible to state that the pressure gradient between the microphones is small. This condition is reported in Equation (4) in which k represents the wave number.

$$I(f) = \frac{[G(f)_{1,2}]}{2\pi f \rho \Delta r} \qquad k\Delta r << 1 \tag{4}$$

Given the theoretical background, it is clear that before proceeding with the sound intensity measurement, it is necessary to address any intrinsic phase mismatch between the microphones [10–12]. With "intrinsic", we refer to the phase mismatch that the two microphones carry as a bias error and therefore is not linked to the pressure difference generated by the measurement itself. Current calibration methods are highlighted in [13–16]. This paper aims at designing a cost-effective phase calibrator to evaluate the phase mismatch between two generic class-1 microphones, not intended for intensity measurements.

2. Materials and Methods

The main concept behind the design of the phase calibrator is exposing the two microphones to the same acoustic field to extract the intrinsic phase difference between them. Following a definition of the numerical model to understand the behavior of the acoustic volume of the calibrator, a prototyping phase started; both microphones and speakers were chosen given their frequency response, geometric characteristics and cost. The last step was the testing of the system to provide for some refinements that led to the final product. The milestones of the project were the following:

- Definition of the numerical model to understand the behavior of the acoustic model with respect to the internal geometry of the calibrator;
- Microphones and speaker choice for frequency range and geometric references;
- Calibrator geometry design, prototyping and software implementations;
- Phase difference extraction and configuration refinements;
- Final configuration definition.

2.1. Numerical Model Definition

In order to design a calibrator that allowed the two microphones to be exposed to the same acoustic field, numerical simulations were carried out as frequency responses until about 3500 Hz, comparing the differences in terms of amplitude and phase expected at

microphone locations. Those are the minimum differences we can expect to measure in a nominally perfect calibrator (with no geometry tolerances due to production process) characterized by those geometries and measured by two perfectly matched microphones. Numerical acoustical FEM models of the calibrator configurations were implemented using commercial software originally intended for structural applications [17]. This approach relies upon the so-called structural–acoustic analogy, which provides the possibility of relating structural displacements to acoustic pressure [18]. Let us consider the standard scalar wave Equation (5), which can be written in the Cartesian coordinates Equation (6):

$$\nabla^2 p = \frac{1}{c^2}\frac{\partial^2 p}{\partial^2 t} \tag{5}$$

$$\frac{\partial^2 p}{\partial^2 x} + \frac{\partial^2 p}{\partial^2 y} + \frac{\partial^2 p}{\partial^2 z} = \frac{1}{c^2}\frac{\partial^2 p}{\partial^2 t}. \tag{6}$$

Equation (6) can be easily reconducted to Equation (7), which represents the stress equilibrium in materials for a given direction.

$$\frac{\partial \sigma_{xx}}{\partial x} + \frac{\partial \tau_{xy}}{\partial y} + \frac{\partial \tau_{xz}}{\partial z} = \rho_s \frac{\partial^2 u_x}{\partial^2 t} \tag{7}$$

Equations (6) and (7) are similar if we consider that:

$$\sigma_{xx} = \frac{\partial p}{\partial x}; \tau_{xy} = \frac{\partial p}{\partial y}; \tau_{xz} = \frac{\partial p}{\partial z}; \rho_s = \frac{1}{c^2}; u_x = p. \tag{8}$$

Therefore, by applying the structural–acoustic analogy, it is possible to deploy an FEM formulation that is described, for the acoustic case, by Equation (9), in which $[M_a]$ and $[K_s]$ represent, respectively, an acoustic mass and stiffness matrix, while F represents the excitation force on the system.

$$[M_a]\ddot{p} + [K_s]p = F \tag{9}$$

To build the matrices in Equation (9), it is necessary to define the physical properties of the fluid nodes of the model [19]. The fluid volume has been meshed with CTETRA elements, whose size was chosen according to the model's required frequency range, which is spaced from [500–3500] Hz. CTETRA elements (3D solid elements) require a PSOLID property (primary property entry) that refers to a MAT110 card that defines the bulk modulus and other properties of the fluid such as density and speed of sound. Generally speaking, the acoustic field inside of the calibrator, generated from an excitation produced by a loudspeaker, could be modeled as an acousto-structural problem in which the motion of the membrane excites the calibrator's internal volume. In this specific case, to simplify the calculation, the membrane motion has been excluded from the model and the external acoustic load has been applied directly to constrained fluid nodes of the regions in which the speaker is supposed to be positioned. Let us notice that the exciting force has been considered unitary and constant throughout the frequency spectrum. The applied method requires also boundary conditions. In this case, the solid wall condition (no flow occurs across the boundary; pressure gradient equal to zero) appeared to be coherent with the phenomenon. The solution of choice was the SOL108, which implements a direct frequency response analysis. Let us notice that the microphones were modeled as fluid volume indentations on the face opposing the loudspeaker, with nodes for phase and amplitude evaluation applied in the center part of the indentation itself and on eight surrounding points.

To summarize, the model characteristics were the following:

- Cylindrical and rectangular geometry as reported in Figures 1 and 2;
- Simplified geometry of the acoustic volume;

- Solid CTETRA fluid nodes elements;
- Rigid wall boundary condition;
- Imposed pressure on constrained nodes to model the acoustic load;
- SOL108—Direct Frequency Response Analysis.

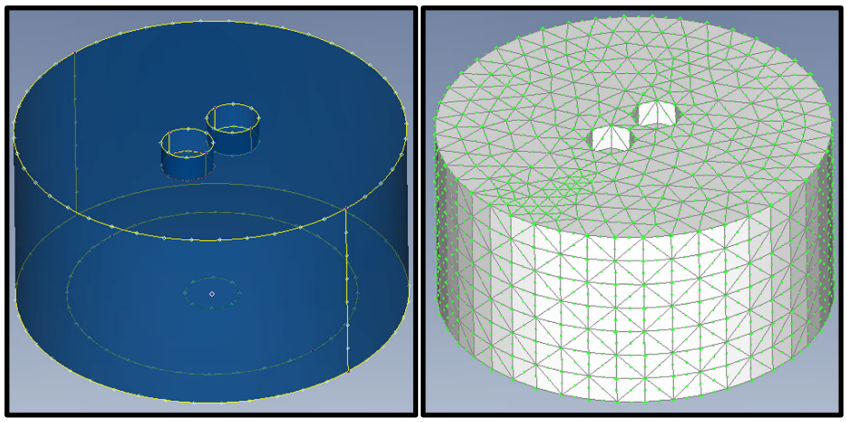

Figure 1. Cylindrical calibrator FEM model.

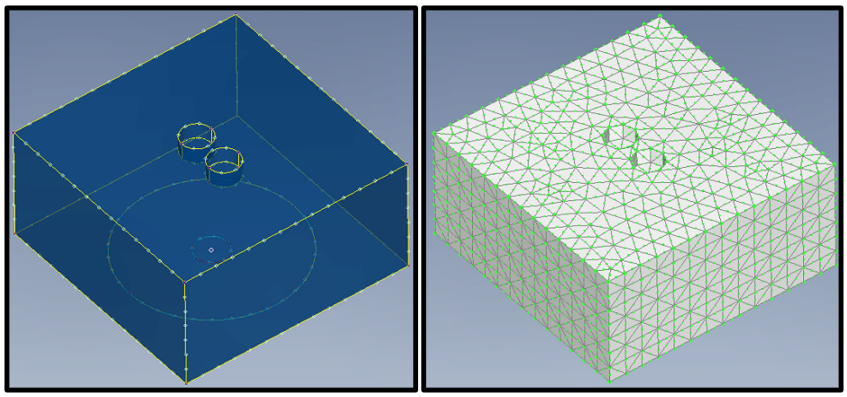

Figure 2. Rectangular calibrator FEM model.

By way of illustration, we have provided a detailed analysis of the response behavior of the acoustic volume in terms of amplitude and phase differences as evaluated in correspondence with the fluid nodes that model the microphones in the [1000–3500] Hz frequency range. We have, therefore, decided to provide the frequency response functions as averaged on the nine points (one central point and eight surrounding points) that meshed the acoustic volume indentation representing the microphones themselves. The cylindrical configuration was the one of choice for this operation.

Figures 3–5 show the amplitude, the amplitude ratio and phase of the frequency response function associated with the cylindrical configuration in the [1000–3500] Hz frequency range. It is possible to notice an occurrence of possible acoustic volume mode shapes around 1500 Hz and 2500 Hz. This eventuality can also be emphasized in the experimental results for which similar behavior can be found around 1500 Hz and 2500 Hz. The deviation of the experimental results from the numerical simulation could be due to non-linearities that were not included in the model and other factors such as local roughness of the material and non perfectly rigid wall of the physical calibrator itself. It is interesting to notice that even at probable resonances of the volume, the microphone's response is almost overlapped.

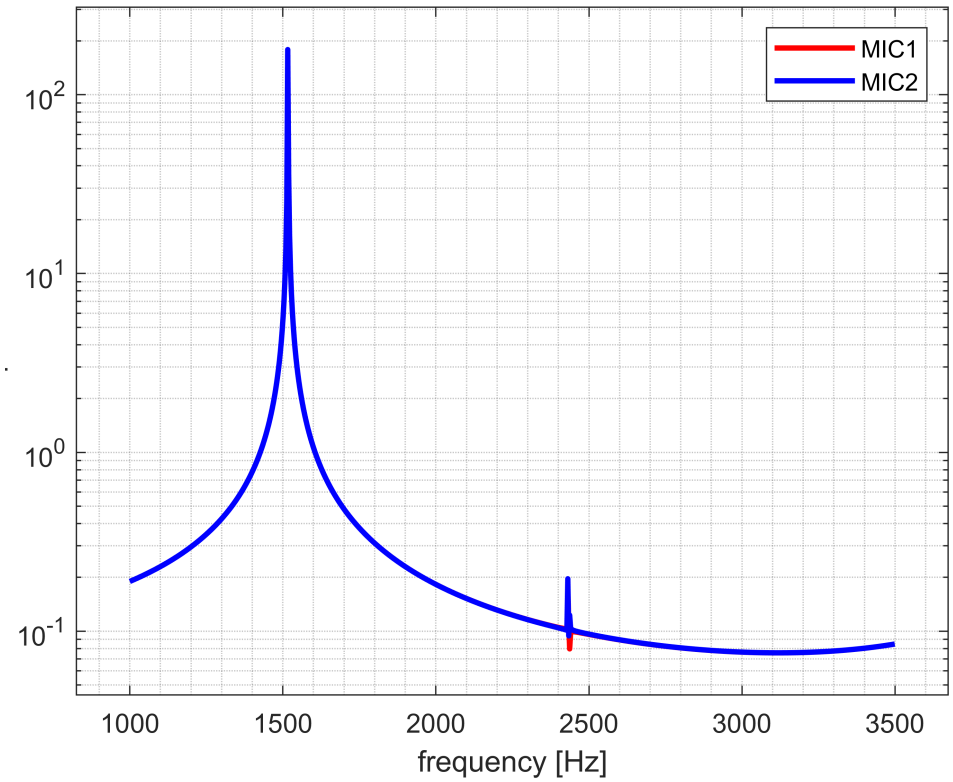

Figure 3. Cylindrical calibrator FRF [1000–3500] Hz—Amplitude.

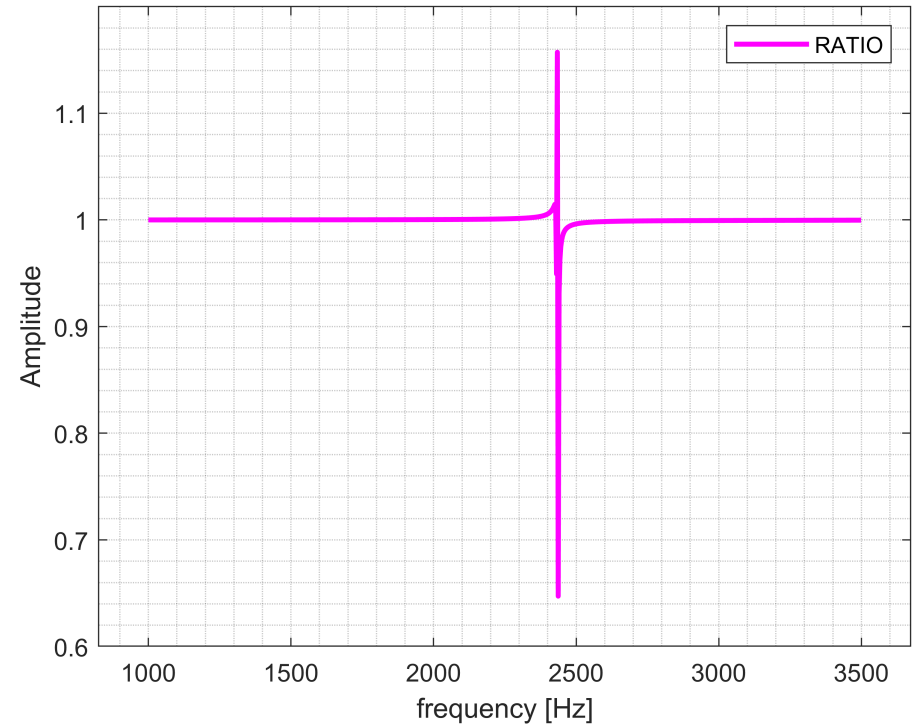

Figure 4. Cylindrical calibrator FRF amplitude ratio [1000–3500] Hz.

As from the previous graphs, those differences are very small (if compared to the total value of the acoustic field measured) in terms of amplitude and are numerically neglectable in terms of phases. This result was in some way expected to be the acoustic wavelength

($\lambda = C/f$ where C is the acoustic wave speed in air and f is the frequency) bigger than the microphone's membrane diameter in the investigated frequency range.

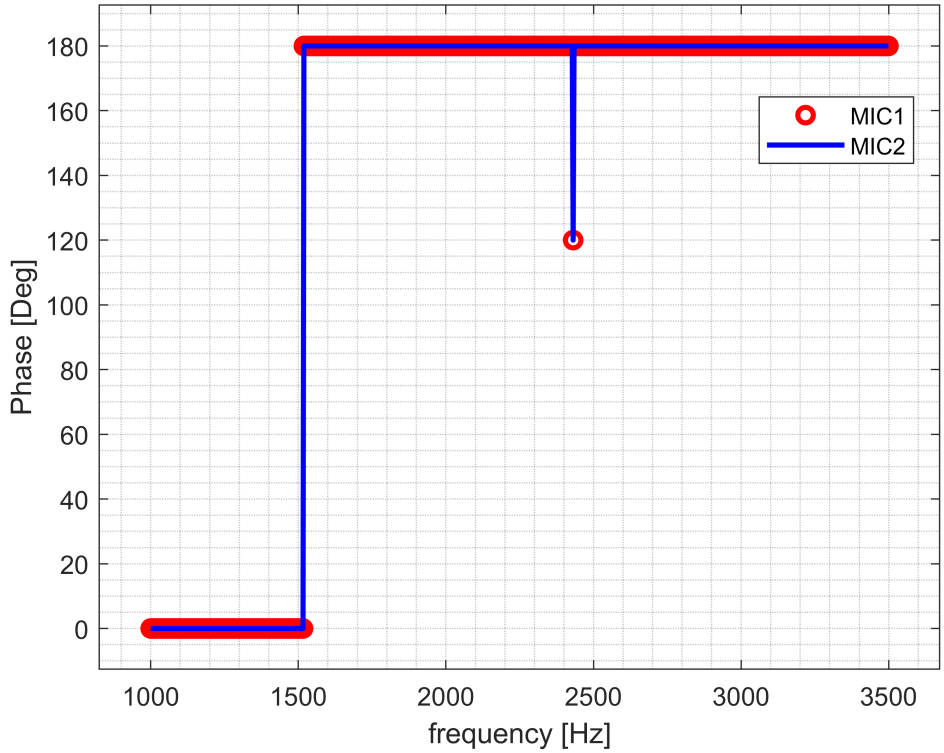

Figure 5. Cylindrical calibrator FRF [1000–3500] Hz—Phase.

Let us notice that, as reported in Figures 6–9, the microphones are exposed to the same acoustic field in the over-mentioned frequency range. As a final result of the numerical investigation, it resulted that within the frequency range considered, both cylindrical and parallelepiped calibrators' shapes had a very low effect on the acoustic differences expected on the two microphone locations, and, as a consequence, both shapes were produced and tested.

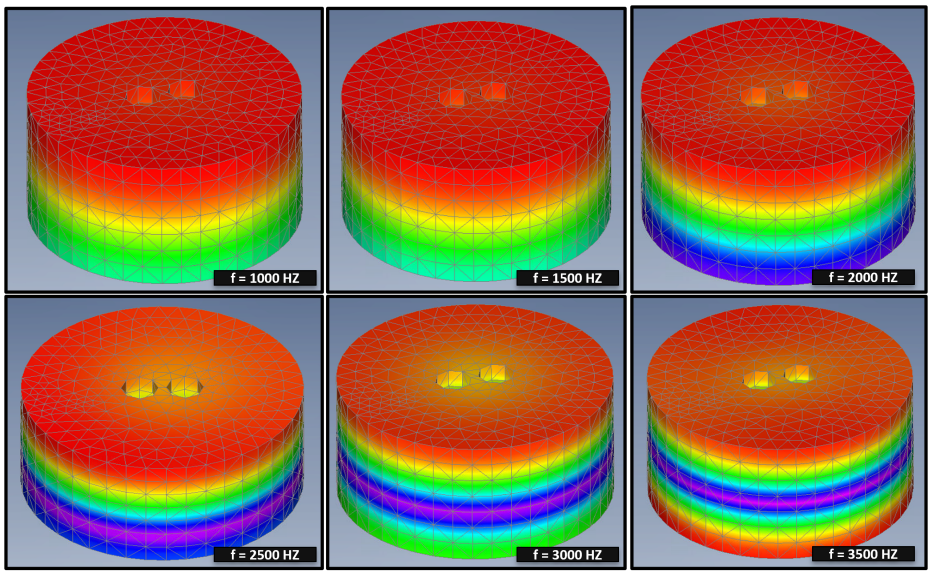

Figure 6. Cylindrical calibrators' pressure ISO surface for microphone exposition evaluation—general view.

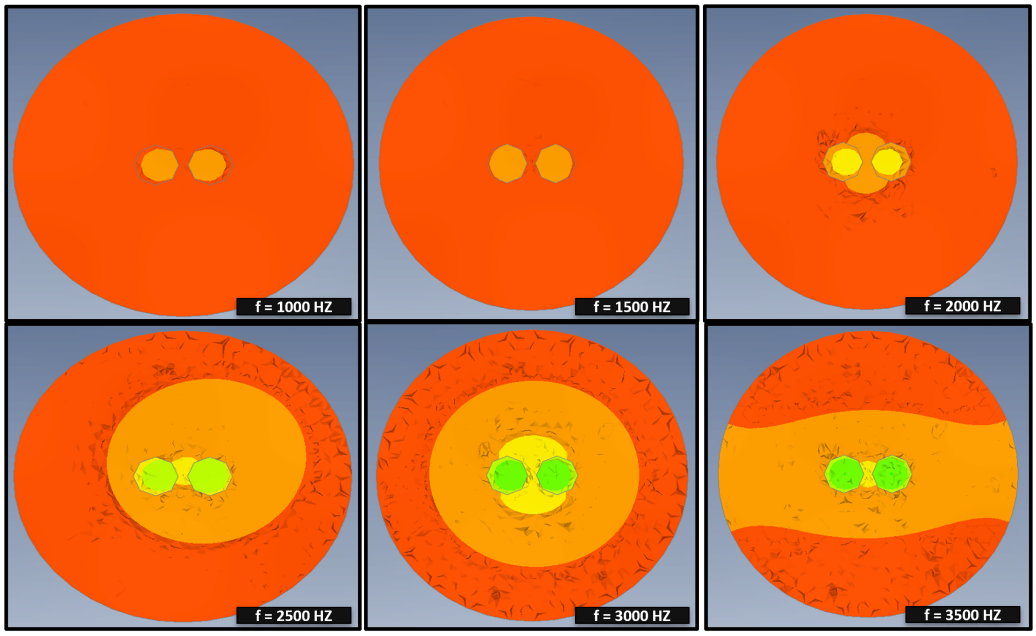

Figure 7. Cylindrical calibrators' pressure ISO surface for microphone exposition evaluation—top view.

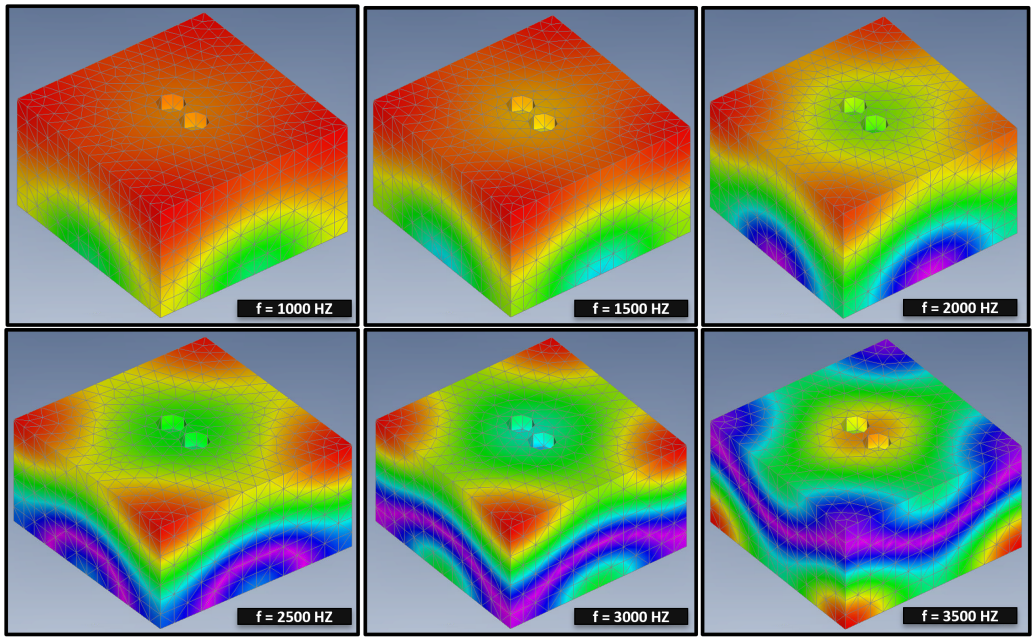

Figure 8. Rectangular calibrators' pressure ISO surface for microphone exposition evaluation—general view.

2.2. Hardware Set-Up and Calibrator Prototyping

A crucial step toward the creation of an acoustic calibrator is the choice of proper hardware for both the signal generation and acquisition system. The signal generator system was implemented by feeding the speaker with a HiFi power amplifier. The signal was generated with a laptop. The data acquisition system was entirely based on NI products. In particular, the measurements were performed with an NI 9234 Sound and Vibration Module managed by a Compact Daq chassis [20]. An acoustic calibrator [21] was deployed to perform level calibration [22] on both microphones. We decided to opt for a conic speaker that provides good linearity in the [100–5000] Hz frequency range. Both the geometric

characteristics, the speaker emission pattern and its frequency response are reported in Figures 10 and 11.

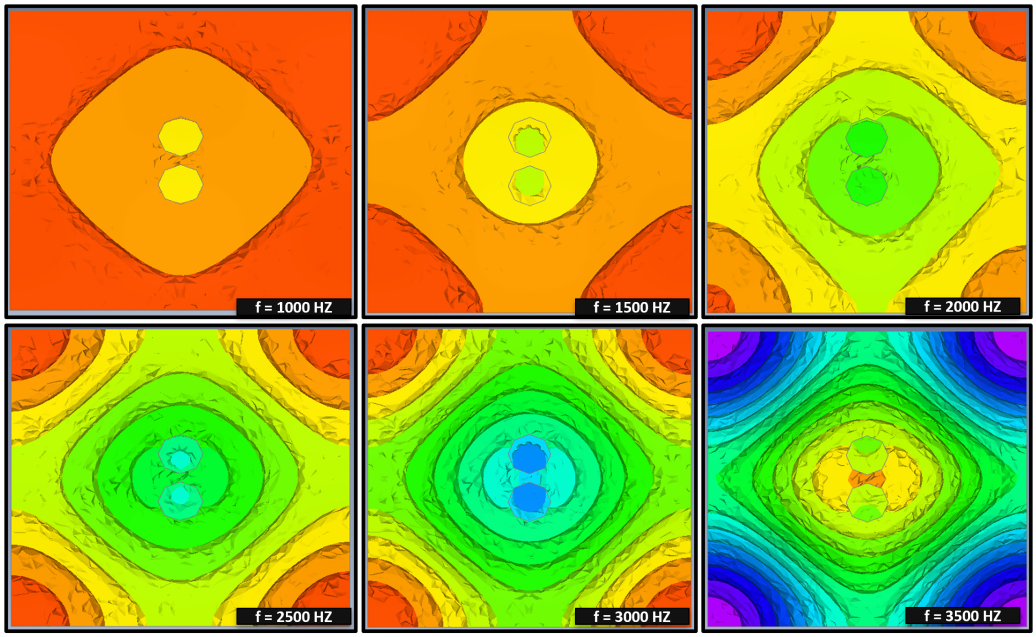

Figure 9. Rectangular calibrators' pressure ISO surface for microphone exposition evaluation—top view.

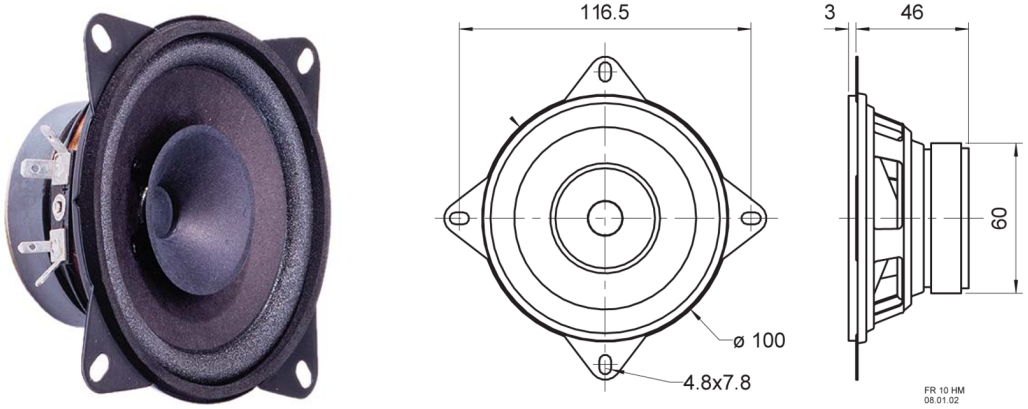

Figure 10. Conic speaker and geometrical characteristics.

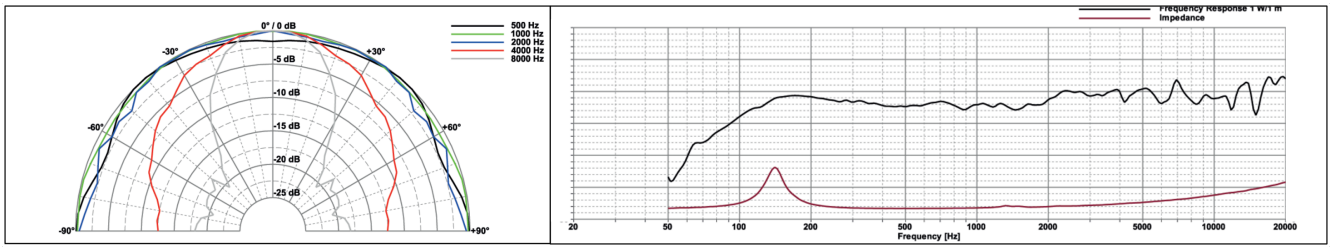

Figure 11. Speaker emission path and frequency response.

As already stated, the aim of the paper was the definition of an acoustic phase calibrator for the evaluation of the phase mismatch of two Class-1 generic microphones not specifically intended for intensity measurements. To fulfill the requirement, we have agreed

to choose two 0.5″ declared 50 mV/Pa ICP microphones that showed good linearity in the [20–12,000] Hz range [23], Figures 12 and 13.

Figure 12. Class-1 0.5″ declared 50 mV/Pa microphones.

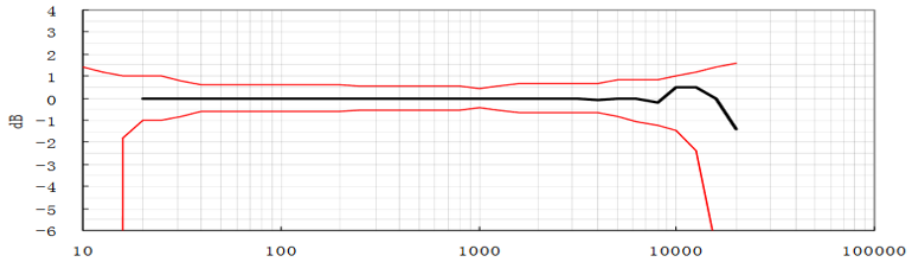

Figure 13. Microphones' typical free-field frequency response function (FRF).

Given the results of the numerical model, two basic geometries analyzed in the numerical model section were implemented to create some physical prototypes (Figures 14 and 15). The calibrators were produced by an AM 3-D printer fed with PLA or ABS filaments. These materials are very cost-friendly and allow for rapid prototyping. Two basic configurations were implemented: A, which resembles a cylindrical geometry and B, which is rectangular. Let us notice that the components are modular, so it was possible to test different caps. In both cases, the acoustic volume was 10 cm in diameter/side and had a 5 cm height.

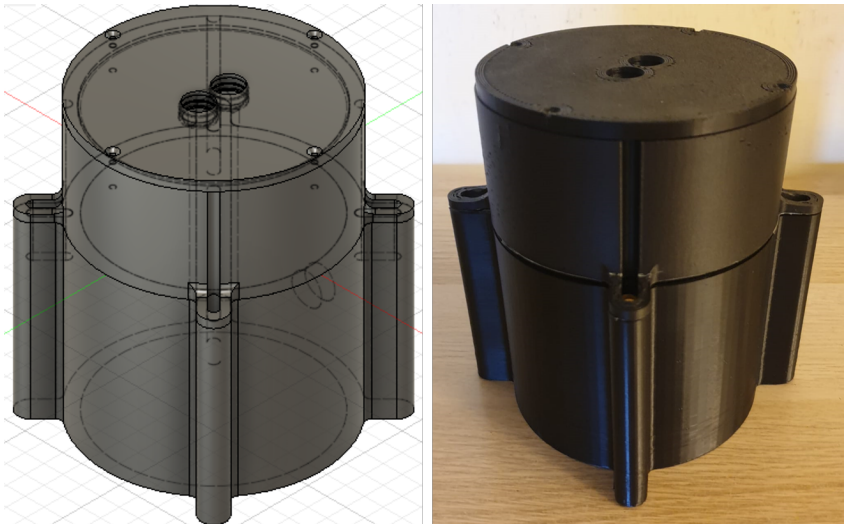

Figure 14. Calibrator. prototype—Configuration A.

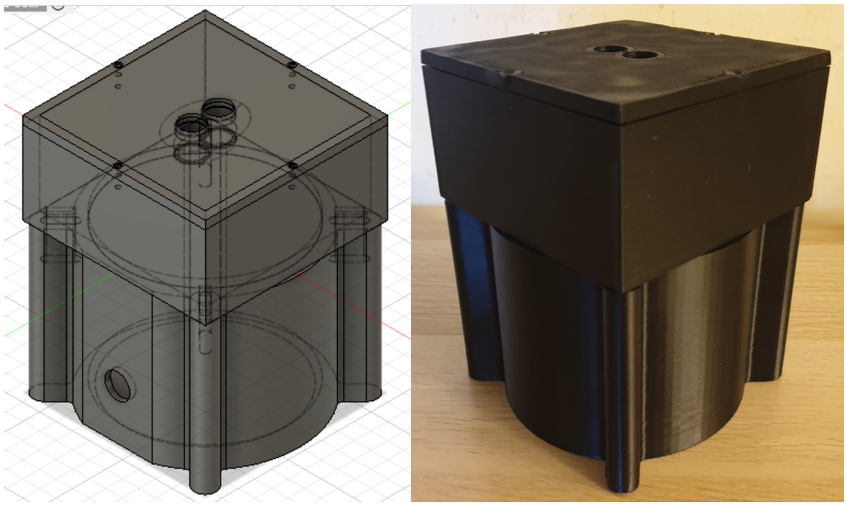

Figure 15. Calibrator prototype—Configuration B.

The chosen configurations have also been implemented in 3 versions, which are resumed in Table 1.

Table 1. Prototype configuration and versions.

Configuration	Characteristics
Configuration A S-S	Side-to-side 16 mm spaced microphones
Configuration A F-F	Face-to-face tightly spaced microphones
Configuration B S-S	Side-to-side 16 mm spaced microphones

Drafts of the calibrators' caps are highlighted in Figures 16–19.

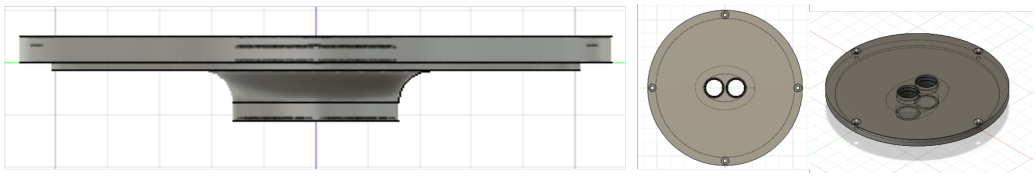

Figure 16. Calibrator cap prototype—Configuration A S-S.

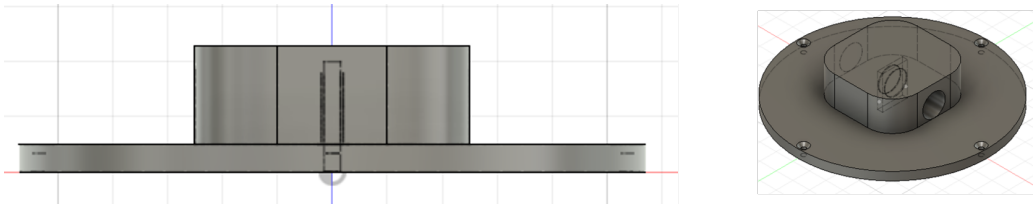

Figure 17. Calibrator cap prototype—Configuration A F-F.

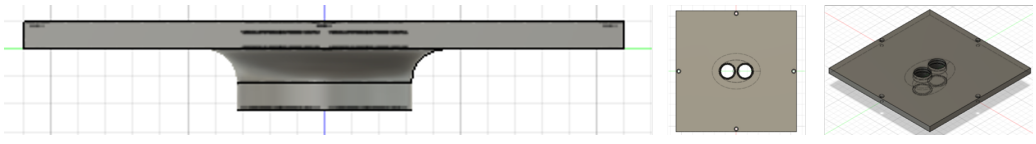

Figure 18. Calibrator cap prototype—Configuration B S-S.

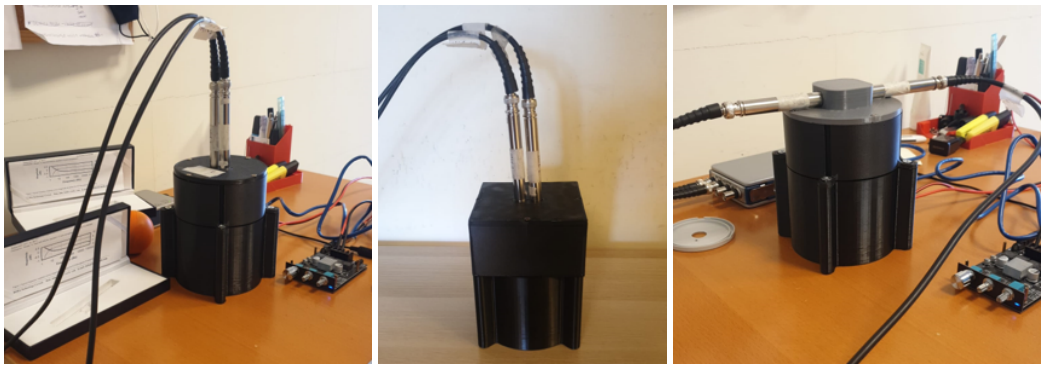

Figure 19. Detail of the positioning of the microphones into the calibrator's cap.

2.3. The Software Implementation

The software, implemented in LabVIEW, was designed to extract the phase difference between the microphones. It was allowed to change the averaging parameters in terms of mathematical formulation (RMS, peak-to-peak, crest, etc.) and number of averages as reported in Table 2. To test the software core capabilities, a simulation version with both generating and acquiring modules was designed. We simulated the microphones with two sine signals with a certain amount of noise. These two signals were 180 degrees out of phase.

Table 2. Final sotware modules and capabilities.

Module	Scope
Calibration module	Phase correction calculation
FFT module	Single signal analysis
Measurement module	Measuring of corrected phase mismatch

From Figure 20, it is evident that the software was able to detect that the virtually generated 70 Hz sound waves (10% of the amplitude white noise) were 180 degrees shifted, which was the imposed phased difference between the signals. Once the software calculation core was validated, it was necessary to implement the possibility of acquiring the two microphone signals when exposed to the acoustic field. The software is organized into 3 modules. The first two windows are dedicated to phase-mismatch correction by calculating the imaginary part of the cross-spectrum of the two signals. In this case, given the necessary FRF calculation, we decide to provide the possibility of using multiple windowing modes and input/output optimization parameters [24,25]. The last module is implemented to show that with the provided phase correction, the newly corrected phase mismatch becomes theoretically null in the frequency range of interest. In addition to the phase difference and the amplitude ratio, we decided to provide information regarding the coherence between the signals.

$$C = \frac{\left|S_{xy}(\omega)\right|^2}{S_{xx}(\omega)S_{yy}(\omega)} \tag{10}$$

Coherence, defined by Equation (10) in which S_{xy} represents the cross-power spectral density between two signals $x(t)$ and $y(t)$, and S_{xx} and S_{yy} are the power spectral density of signal $x(t)$ and $y(t)$, is a statistical measurement that expresses the level of linear dependency between two ergodic signals. It is a real number ranging from 0 to 1 that represents the possibility of obtaining one signal from another through a linear filter. Coherence can therefore be intended as a measurement of the linearity of a system and a measurement of how a certain peak can represent a mode shape of the system rather than measurement noise.

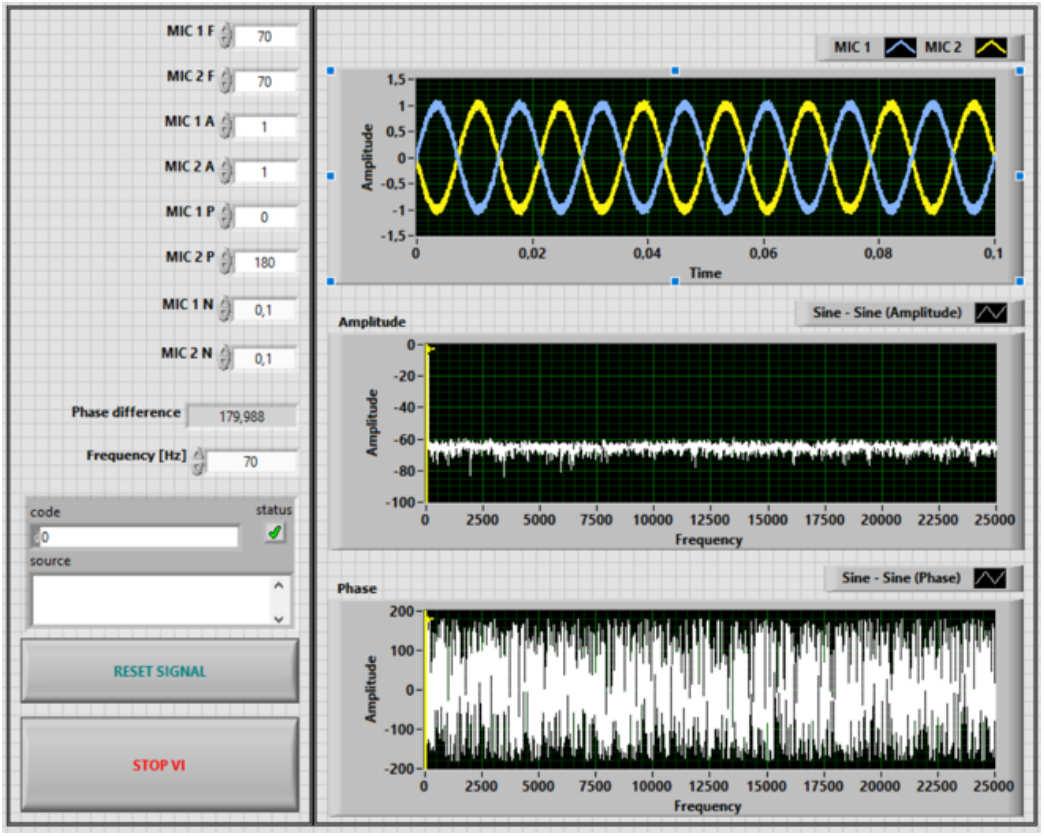

Figure 20. Test version of the software.

The acoustic signal was generated with Audacity software. In our case, white noise was the signal of choice. This was purely arbitrary since the only needed condition was the equivalent exposure to the same acoustic level of the two microphones. Given the characteristics of the speaker and the physics of the problem, no input/output synchronization was needed.

3. Results

The following section provides an overview of the results of the tests conducted on the three versions of the calibrator, according to Table 1. In each case, the test has been carried out by exposing both microphones to white noise to extract the intrinsic phase mismatch between the microphones and, therefore, determining the required phase correction.

3.1. Configuration A S-S

The first measurement was carried out on the Configuration A S-S calibrator. It is possible to notice that two distinct mode shapes can be highlighted at 2200 and 5800 Hz (Figures 21 and 22). In correspondence with those frequencies, a drop down in coherence was experienced as repoted in Table 3 and Figure 23.

Table 3. Configuration A S-S—test specification and results before calibration.

Test Specification	Results
H2 estimator 30 averages Hanning windowing	Probable distinct modeshapes at 2200 and 5800 Hz Coherence drop at extsimeq 2200 and 5800 Hz Phase differences up to 100 deg

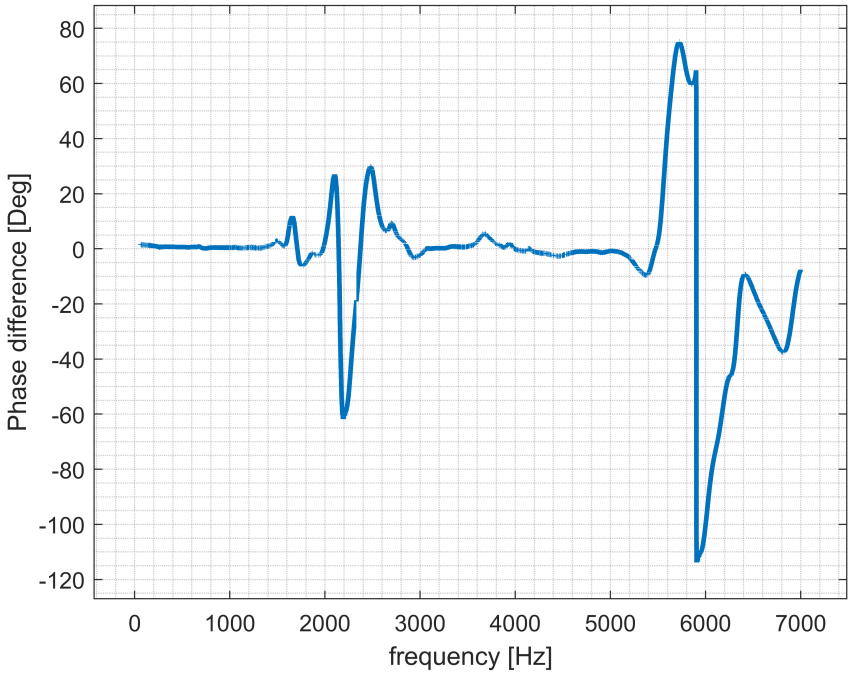

Figure 21. Configuration A S-S—phase difference before calibration.

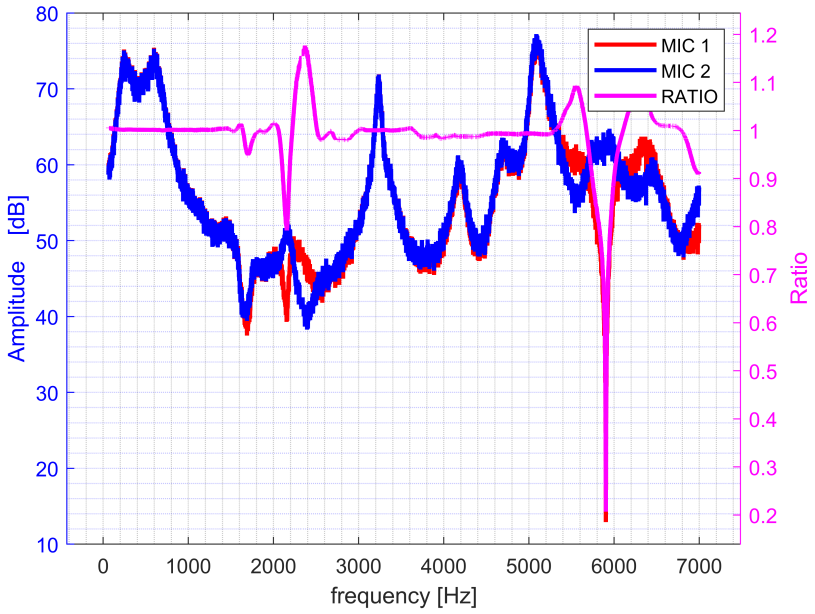

Figure 22. Configuration A S-S—amplitude and ratio.

After the calibration, a maximum phase mismatch of 1 and 10 deg was measured in correspondence with 2200 and 5800 Hz. For the other frequencies, the error was bounded in the [−0.5 0.5] deg range as reported in Table 4 and Figures 24 and 25.

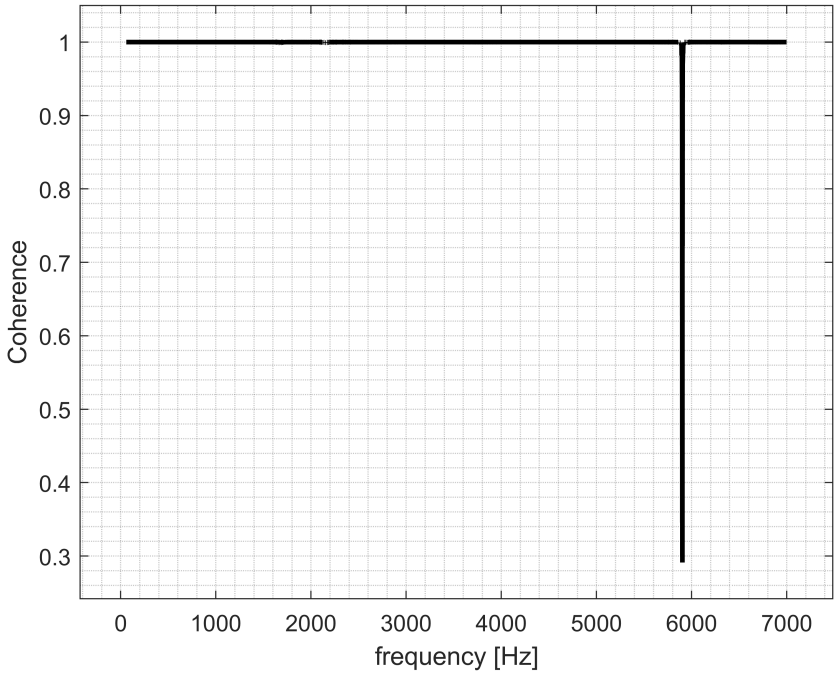

Figure 23. Configuration A S-S—coherence before calibration.

Table 4. Configuration A S-S—test specification and results for calibrated measurement.

Test Specification	Results
H1 estimator	Probable modeshapes at extsimeq 5800 Hz
30 averages	Coherence drop at extsimeq 5800 Hz
Hanning windowing	Phase differences up to 1 deg at extsimeq 2200 Hz
/	Phase differences up to 10 deg at extsimeq 5800 Hz
/	Phase difference bounded [−0.5 0.5] deg in [60–5000] Hz frequency range

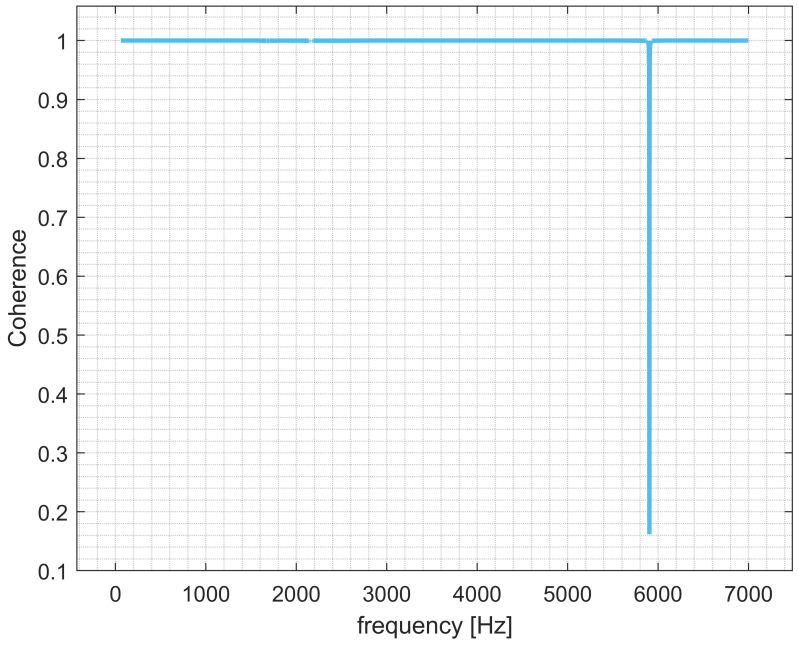

Figure 24. *Cont*.

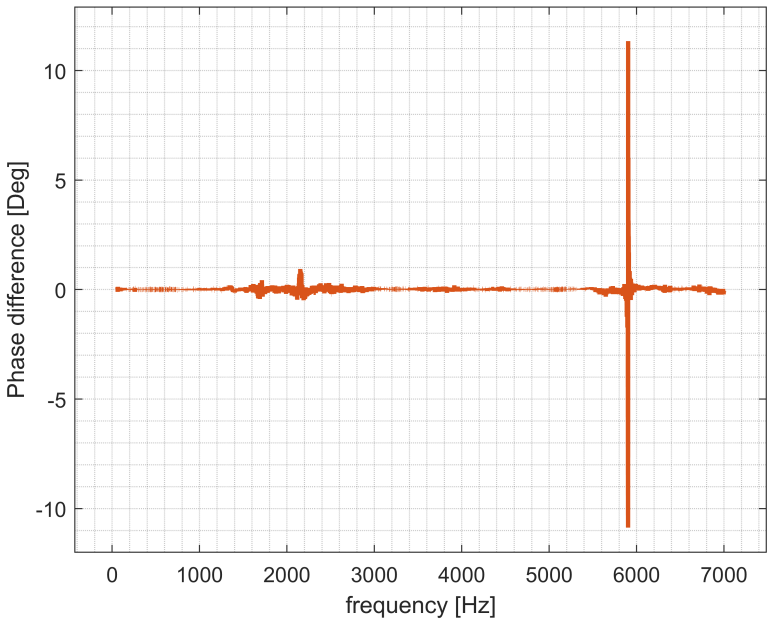

Figure 24. Configuration A S-S—coherence and phase difference for calibrated measurement.

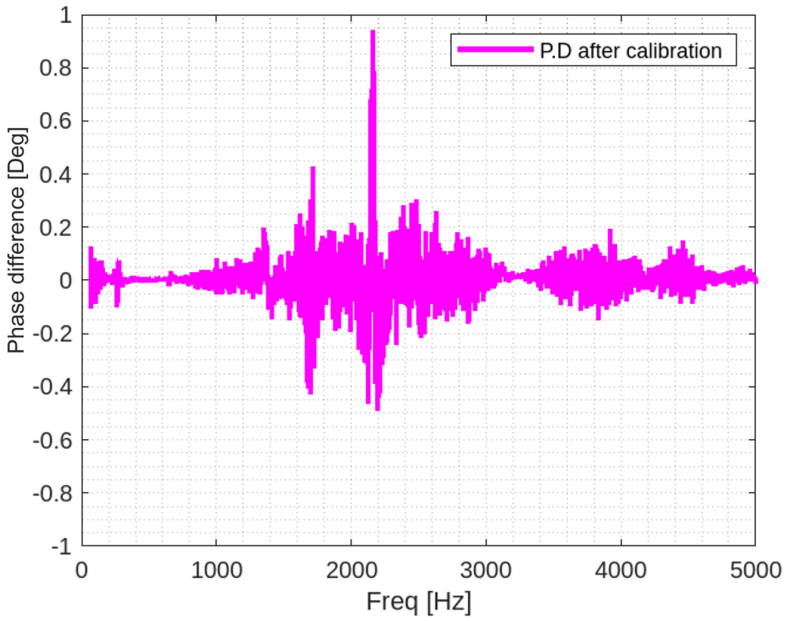

Figure 25. Configuration A S-S—phase difference for calibrated measurement.

3.2. Configuration B S-S

The second measurement was carried out on the Configuration B S-S calibrator. A large phase variability was highlighted in the mentioned frequency ranges as reported in Table 5 and Figures 26–28.

Table 5. Configuration B S-S—test specification and results before calibration.

Test Specification	Results
H2 estimator	Great variability in [1500–2000] Hz and [5000–6500] Hz frequency ranges
30 averages	Phase differences up to 80 deg
Hanning windowing	/

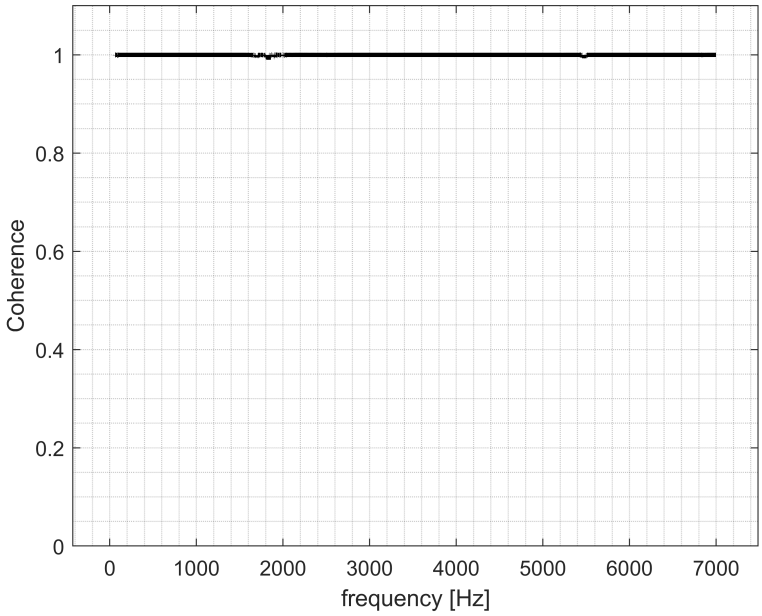

Figure 26. Configuration B S-S—coherence before calibration.

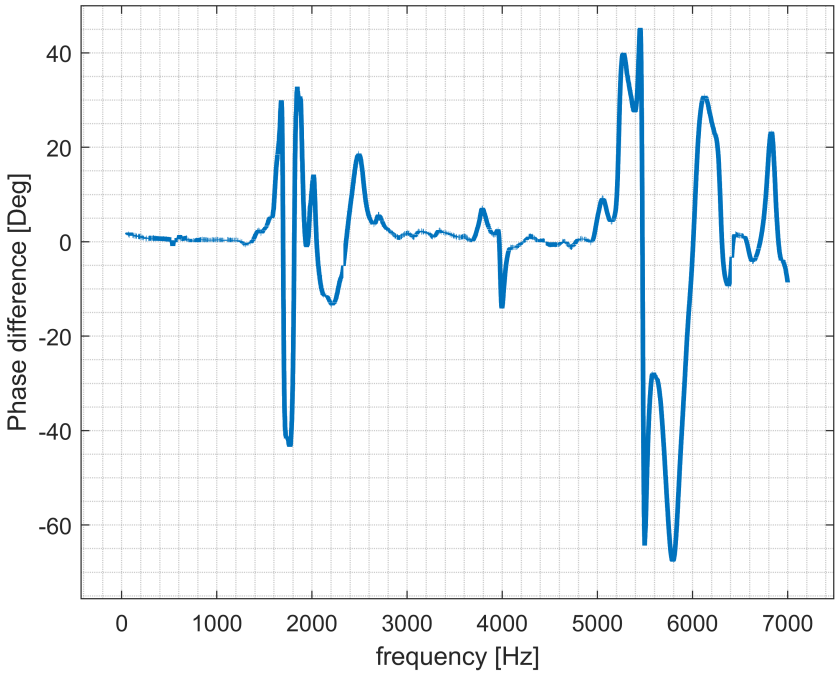

Figure 27. Configuration B S-S—phase difference before calibration.

The B S-S configuration reported a better response regarding maximum phase mismatch. Even if the results were promising, the rectangular was not the configuration of choice given the higher variability of the modes as reported in Table 6 and Figures 29 and 30.

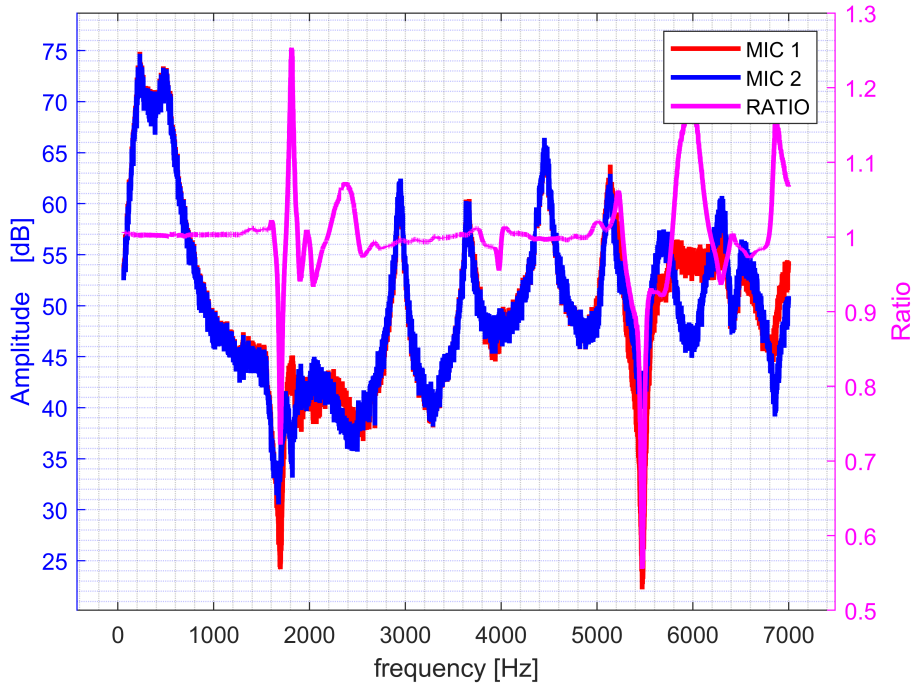

Figure 28. Configuration B S-S—amplitude and ratio.

Table 6. Configuration B S-S—test specification and results for calibrated measurement.

Test Specification	Results
H1 estimator	Phase differences up to −2 deg in [1500–2000] Hz frequency range
30 averages	Phase differences up to 3 deg in [5000–6500] Hz frequency ranges
Hanning windowing	Phase difference bounded [−0.6 0.6] deg in 60–7000 Hz frequency range

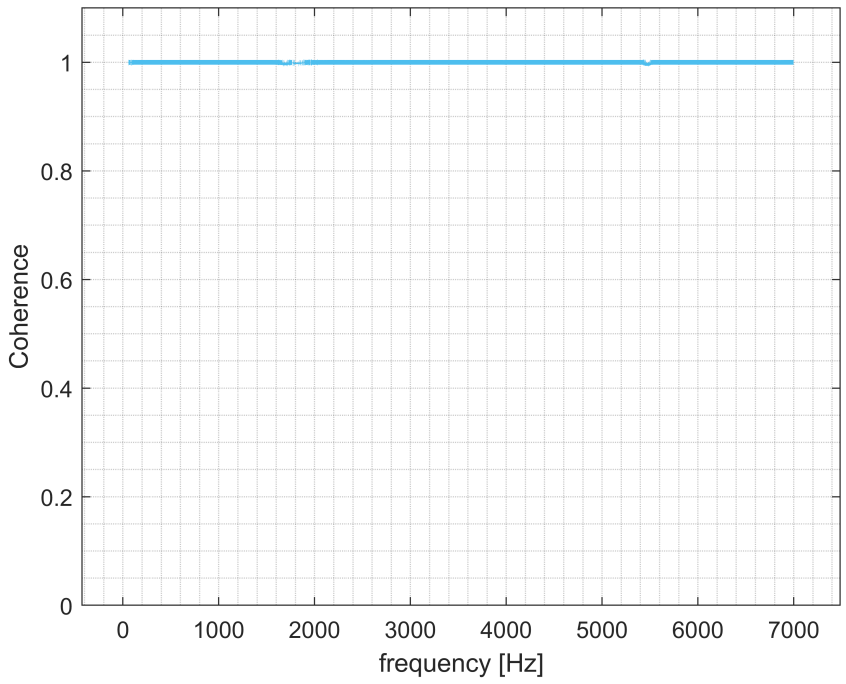

Figure 29. *Cont*.

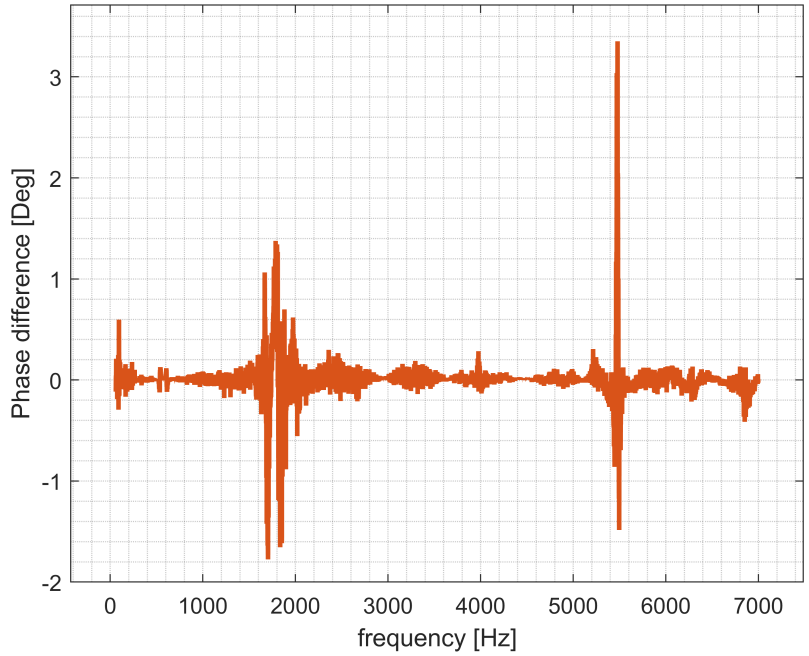

Figure 29. Configuration B S-S—coherence and phase difference for calibrated measurement.

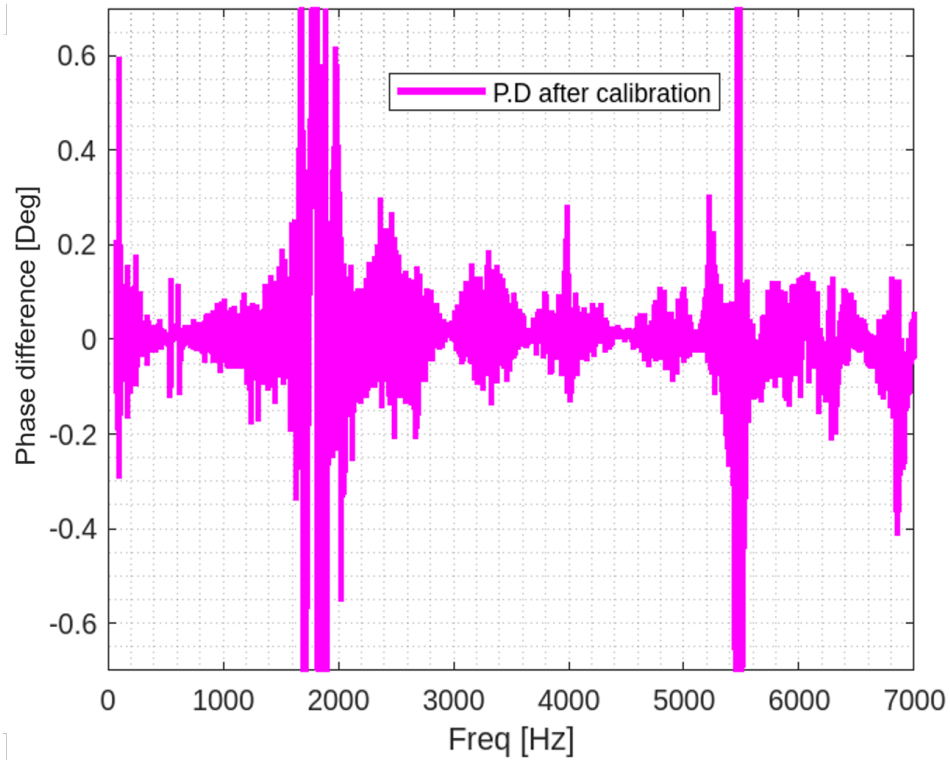

Figure 30. Configuration B S-S—phase difference for calibrated measurement.

3.3. Configuration A F-F

In the case of the A F-F configuration, one-mode shapes can be highlighted at the 4800 Hz frequency range. The maximum measured phase mismatch was 10 deg as reported in Table 7 and Figures 31–33.

Table 7. Configuration A F-F—test specification and results before calibration.

Test Specification	Results
H1 estimator 50 averages Hanning windowing	Phase mismatch peak at 4800 Hz No Coherence drop at 4800 Hz Phase differences up to 10 deg

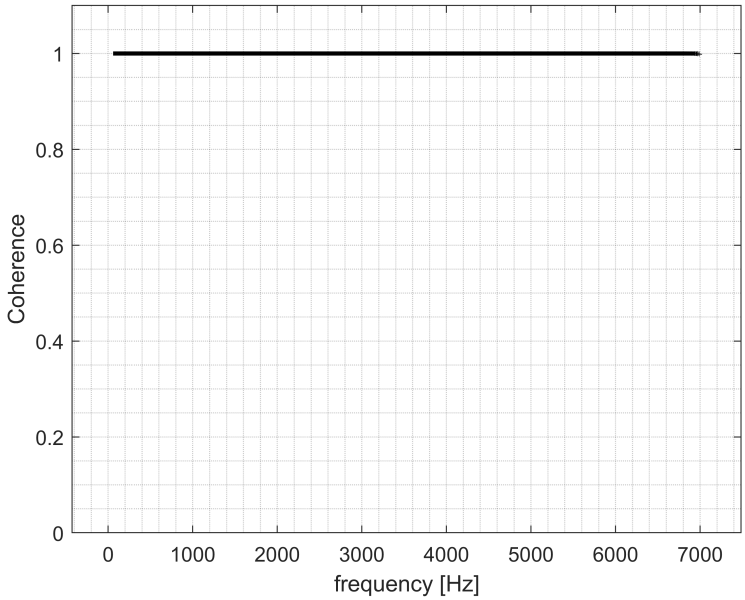

Figure 31. Configuration A F-F—coherence before calibration.

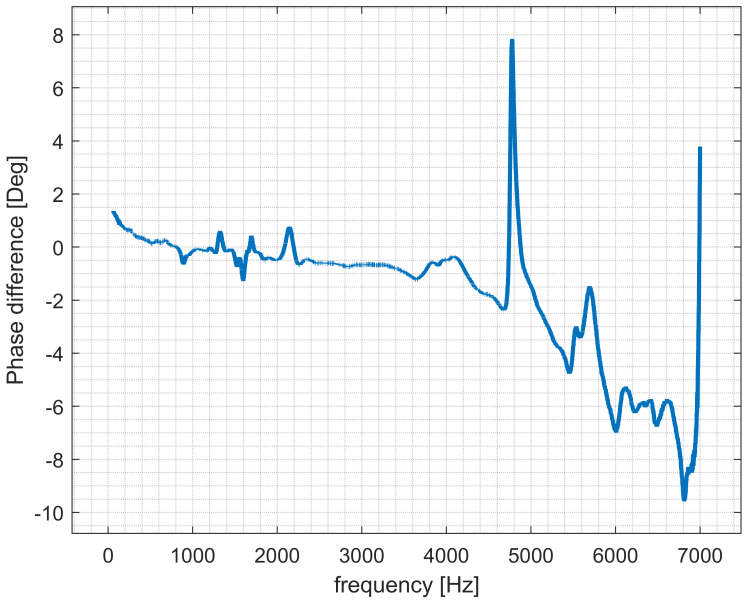

Figure 32. Configuration A F-F—phase difference before calibration.

Let us notice that in this case, the maximum phase mismatch was 0.6 deg. Up to almost 6800 Hz, the signal was bounded in the [−0.2 0.2] deg range. In this case, it was possible to emphasize no phase-mismatch peaks. Given the result, the A F-F configuration was considered the most promising as highlightable in Table 8 and Figures 34–36.

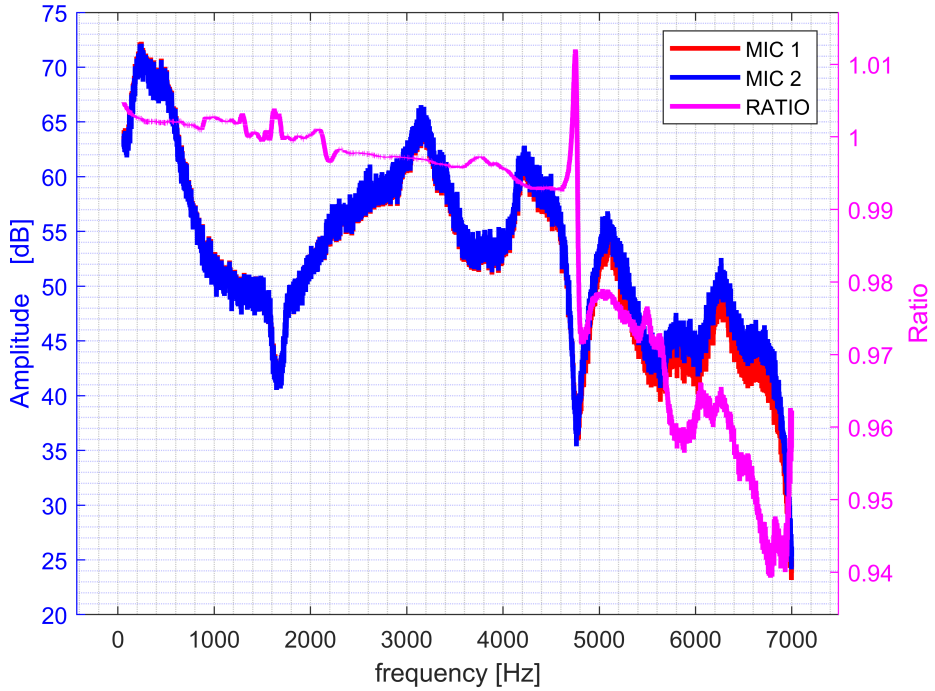

Figure 33. Configuration A F-F—amplitude and ratio.

Table 8. Configuration A F-F—test specification and results for calibrated measurement.

Test Specification	Results
H1 estimator	Phase differences up to 0.6 deg in [60–7000] Hz frequency ranges
50 averages	Phase difference bounded [−0.2 0.2] deg in [60–6800] Hz frequency range
Hanning windowing	/

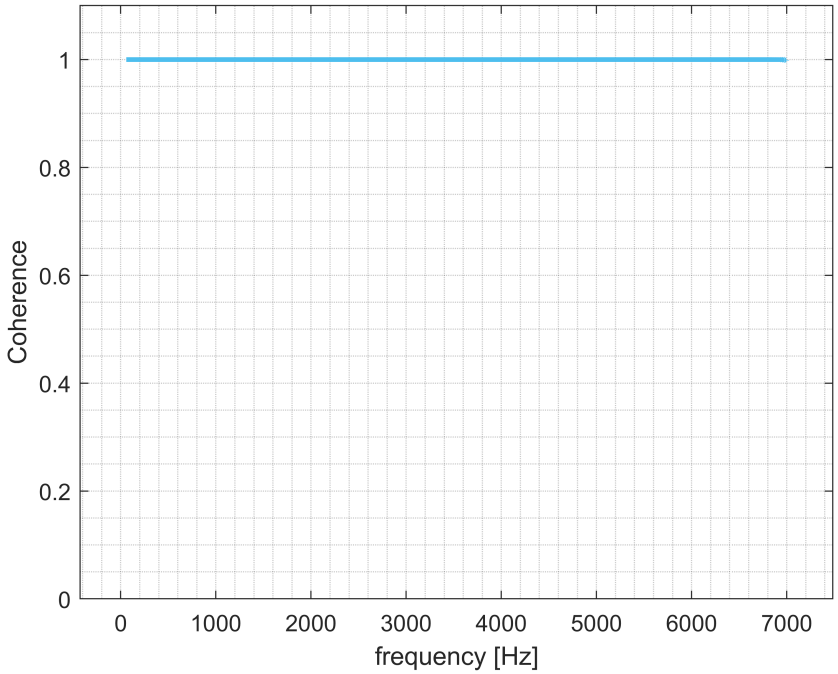

Figure 34. Configuration A F-F—coherence for calibrated measurement.

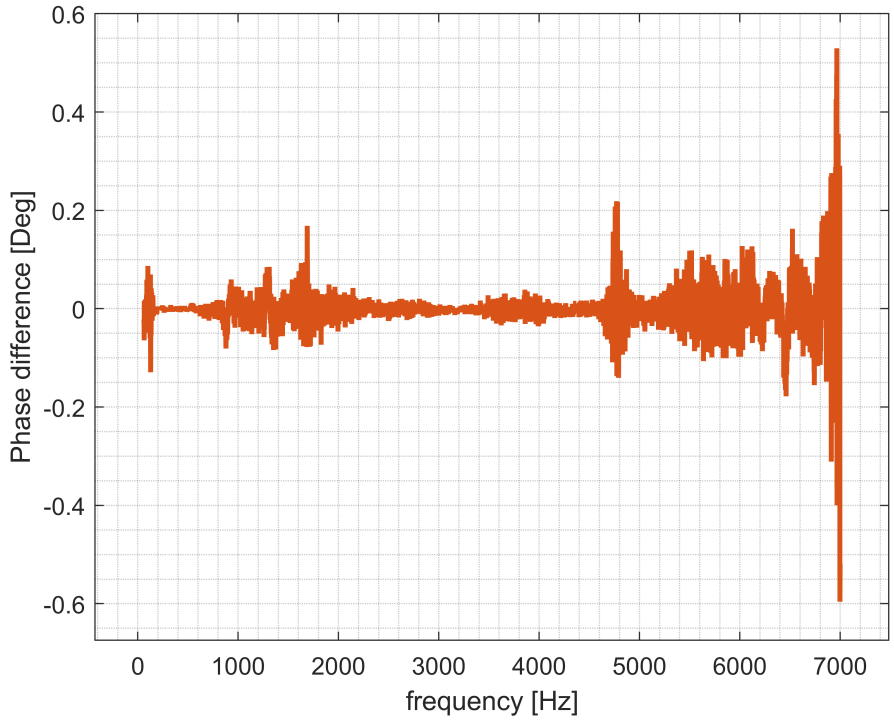

Figure 35. Configuration A F-F—phase difference for calibrated measurement.

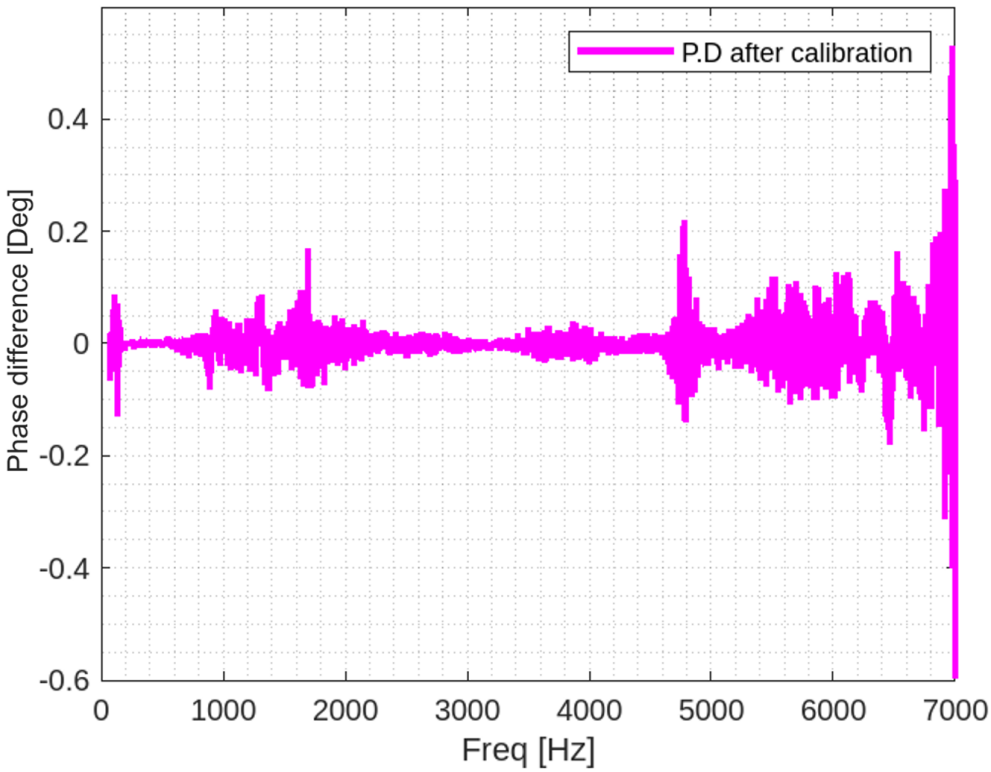

Figure 36. Configuration A F-F—phase difference for calibrated measurement.

4. Further Prototype Implementation and Discussion

Given the results of the measurements performed on the prototypes, configuration A with F-F microphones was the one of choice. The calibrator was scaled into a smaller, more portable version (3 cm diameter) (Figure 37). Both the original and scaled A F-F configurations exhibited good behavior when compared to a state-of-the-art acoustic coupler.

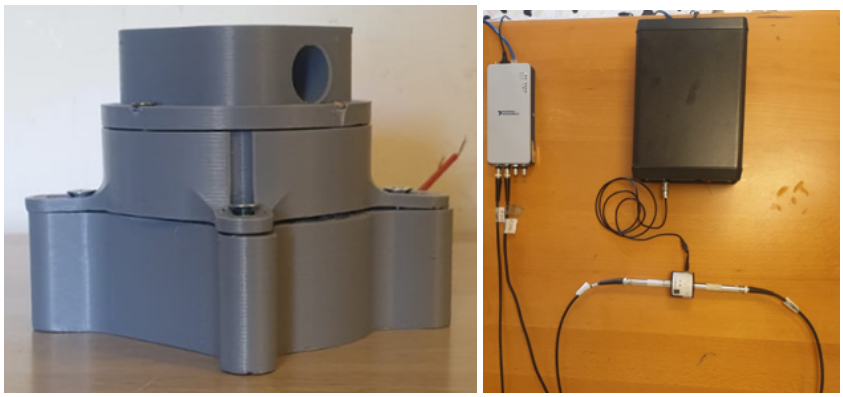

Figure 37. Configuration A F-F, scaled (**left**)—commercial state-of-the art acoustic coupler (**right**).

After proceeding with the calibration, the device showed very good consistency up to 4000 Hz. The result in the [60–4000] Hz frequency range was very satisfying, given that the calibrated phase mismatch is contained in a [−0.02 0.06] deg range. Starting from f > 4000 Hz, the peak phase mismatch is set at 2.5 deg are reported in Table 9 and Figures 38 and 39 .

Table 9. Configuration A S-S, scaled—test specification and results for calibrated measurement.

Test Specification	Results
H1 estimator	Good stability up to 4000 Hz
50 averages	Increasing phase mismatch for f > 4000 Hz
Hanning windowing	Phase differences lesser than 0.06 deg in [60–4000] Hz frequency range

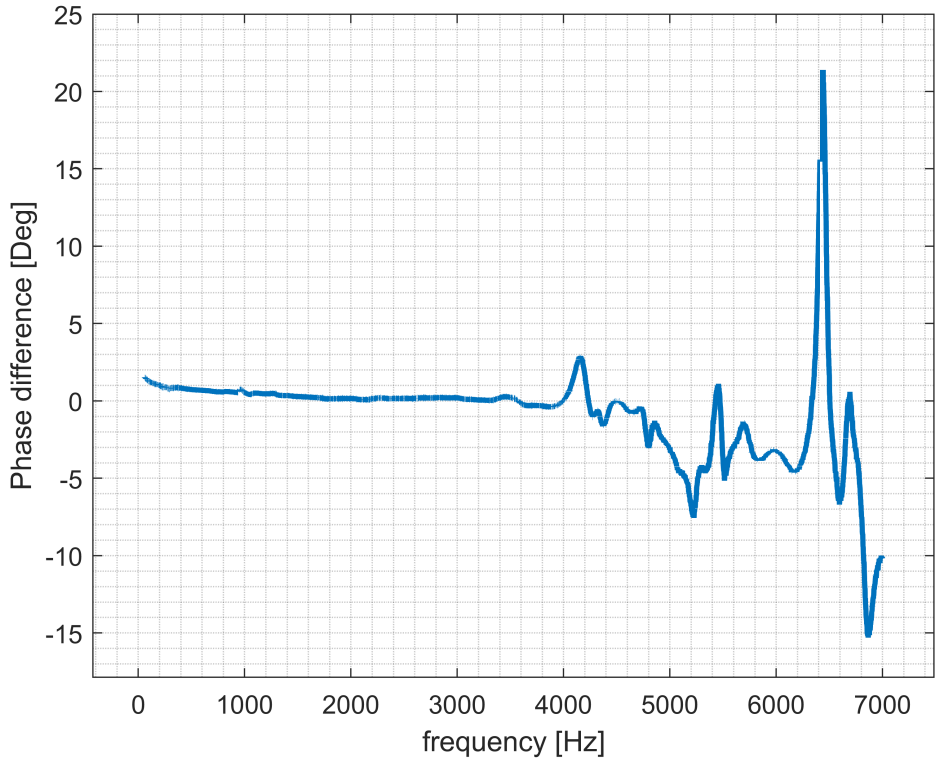

Figure 38. Configuration A F-F, scaled—phase difference for calibrated measurement.

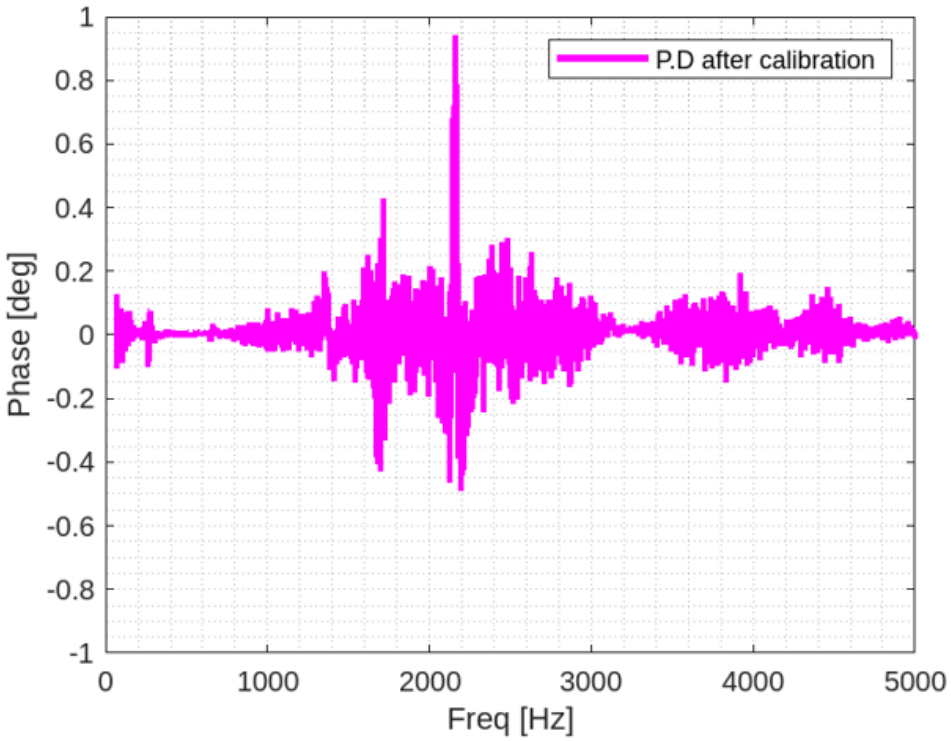

Figure 39. Configuration A F-F, scaled—phase difference for calibrated measurement.

Both the full-size and the scaled configurations showed good results when compared to the acoustic coupler in a [60–7000] Hz frequency range. Clearly, the better results were obtained in the [1000–4000] Hz frequency range, which is the one targeted in the numerical model as reported in Figure 40.

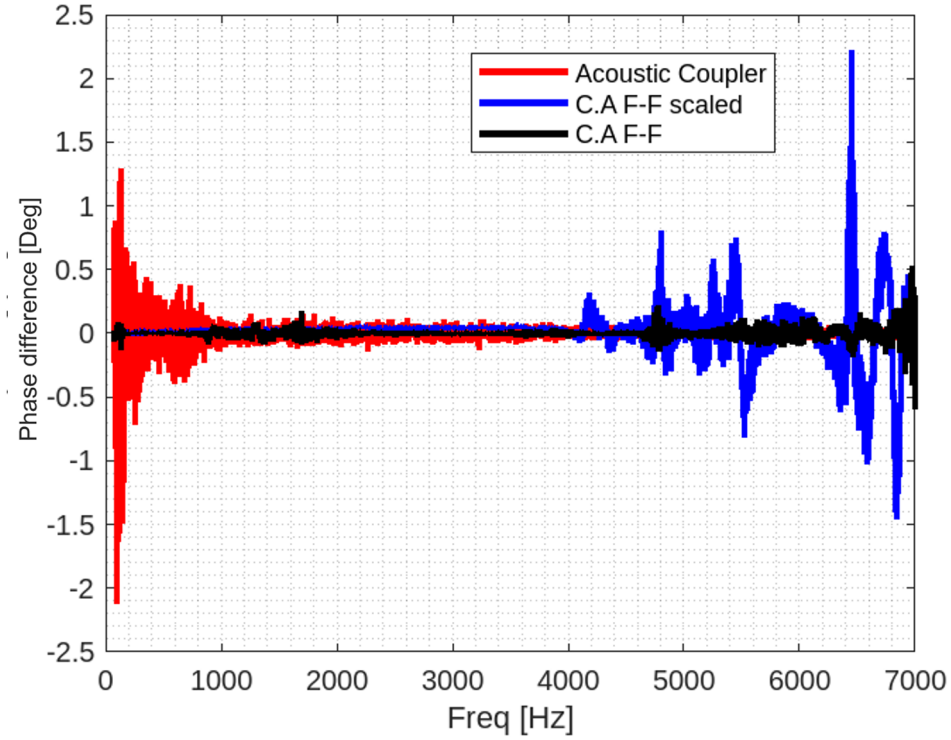

Figure 40. Comparison between the phase difference for calibrated measurement for prototypes and reference instruments in the [60–7000] Hz frequency range.

In the [60–1000] Hz range, both the calibrators showed good results when compared to the reference instrument (Figure 41).

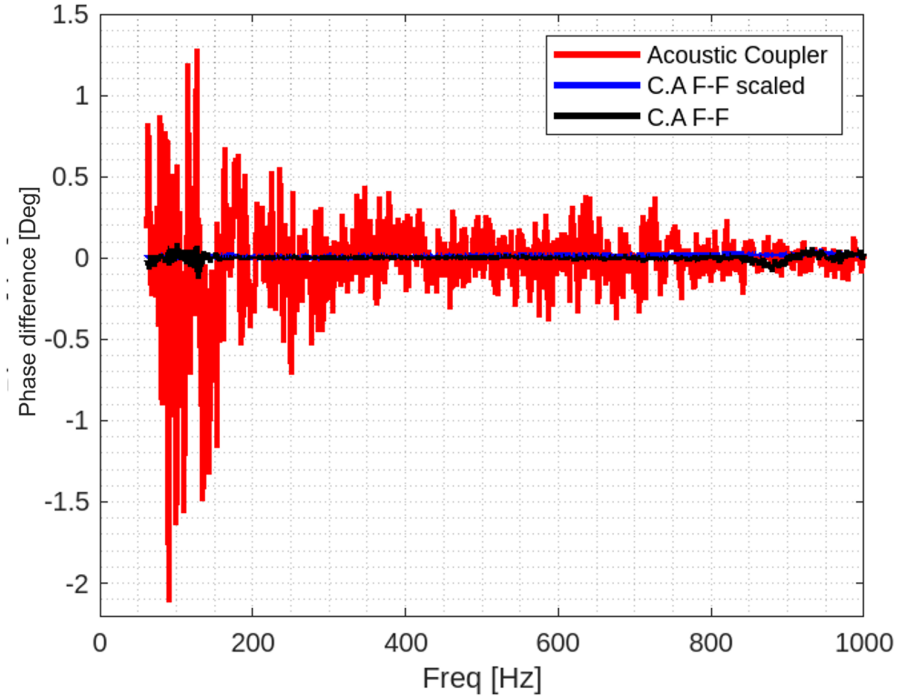

Figure 41. Comparison between the phase difference for calibrated measurement for prototypes and reference instruments in the [60–1000] Hz frequency range.

In the [1000–4000] Hz range, the performances were still very competitive regarding the reference instrument. The phase mismatch of the scaled model suffered from bias error (Figure 42).

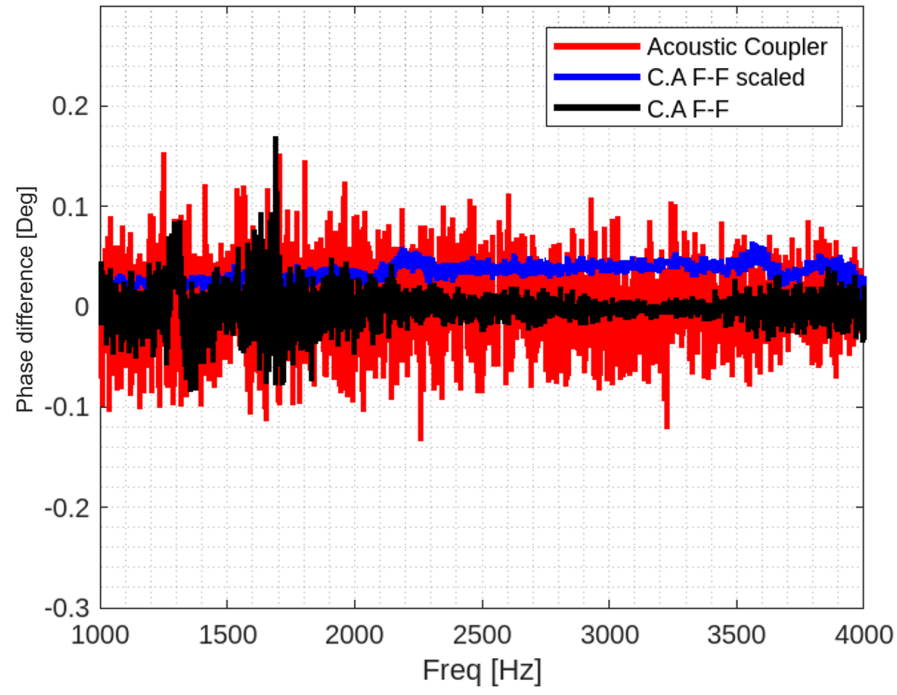

Figure 42. Comparison between the phase difference for calibrated measurement for prototypes and reference instruments in the [1000–4000] Hz frequency range.

In the [4000–7000] Hz frequency range, both the calibrators experienced poor performances when compared to the acoustic coupler (Figure 43).

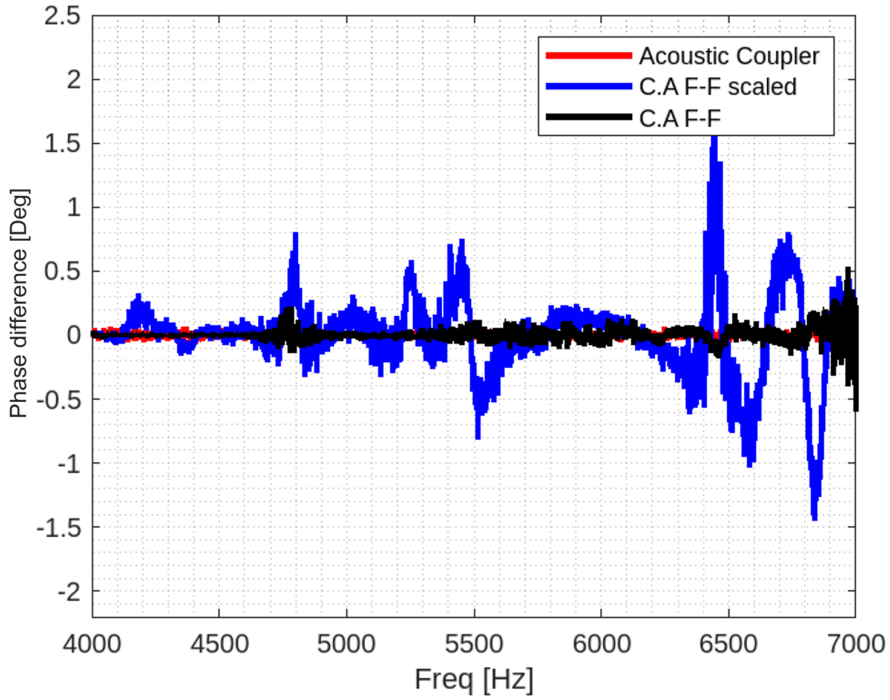

Figure 43. Comparison between the phase difference for calibrated measurement for prototypes and reference instruments in the [4000–7000] Hz frequency range.

5. Conclusions

This work aimed at designing an acoustic phase calibrator to identify phase mismatches between class-1 microphones not intended for intensity measurements and provide the required corrections in a given frequency range. Numerical acoustical FEM simulations were carried out with commercially available numerical codes exploiting the structural–acoustic analogy. The model's results guided the prototyping phase, which led to three different configurations. Tests were conducted employing a specifically designed software that allowed performing both the intrinsic phase-mismatch extraction and correction. The configuration of choice was the cylindrical face-to-face (Configuration A-F-F), which was scaled to provide a more compact solution. Both the full-size Configuration A-F-F and its scaled version were compared with a state-of-the-art, laboratory standard acoustic coupler showing very good results in the [60–4000] Hz frequency range and encouraging one in the [4000–7000] Hz range. Future developments of the calibrator will be oriented to the extension of the frequency range and the creation of a standalone version.

Author Contributions: Conceptualization, N.R. and E.M.; methodology, E.M.; software, N.R.; hardware, A.E.; validation, N.R., E.M. and A.E.; formal analysis, E.M.; investigation, N.R.; resources, E.M.; data curation, N.R., E.M. and A.E.; writing—original draft preparation, N.R.; writing—review and editing, E.M.; supervision, E.M.; project administration, E.M. All authors have read and agreed to the published version of the manuscript.

Funding: This research received no external funding.

Data Availability Statement: Data are contained within the article.

Acknowledgments: Grateful thanks to the Italian company Sonora Srl. for the donation of the materials received for experimental campaigns and for providing expertise concerning both the software and hardware implementation.

Conflicts of Interest: Authors Nicola Russo and Andrea Esposito were employed by the company Sonora Srl. The remaining authors declare that the research was conducted in the absence of any commercial or financial relationships that could be construed as a potential conflict of interest.

References

1. Jacobsen, F. Sound intensity and its measurement and applications. *Curr. Top. Acoust. Res.* **2023**, *3*, 79–91.
2. Crocker, M.; Jacobsen, F. Sound Intensity. *Encycl. Acoust.* **2007**, *4*, 1855–1868.
3. Crocker, M.; Arenas, J. Fundamentals of the direct measurement of sound intensity and practical applications. *Acoust. Phys.* **2003**, *49*, 163–175. [CrossRef]
4. Pope, J.; Hickling, R.; Feldmaier, D.A.; Blaser, D.A. The Use of Acoustic Intensity Scans for Sound Power Measurement and for Noise Source Identification in Surface Transportation Vehicles. *SAE Trans.* **1981**, *90*, 1530–1538.
5. Jacobsen, F.; Cutanda, V.; Juhl, P.M. A numerical and experimental investigation of the performance of sound intensity probes at high frequencies. *J. Acoust. Soc. Am.* **1998**, *103*, 953–961. [CrossRef]
6. Juhl, P.M.; Jacobsen, F. A note on measurement of sound pressure with intensity probes. *J. Acoust. Soc. Am.* **2004**, *116*, 1614–1620. [CrossRef]
7. Kotus, J.; Czyzewski, A.; Kostek, B. 3D Acoustic Field Intensity Probe Design and Measurements. *Arch. Acoust.* **2016**, *41*, 701–711. [CrossRef]
8. *ANSI S1.9-1996 (R2006)*; Instruments for the Measurement of Sound Intensity. ANSI (American National Standards Institute): New York, NY, USA, 1996.
9. Chung, J.Y.; Blaser, D.A. Recent Developments in the Measurement of Acoustic Intensity using the Cross-Spectral Method. *SAE Trans.* **1981**, *90*, 1520–1529.
10. Frederiksen, E.; Piil, M. *Characteristics of Microphone Pairs and Probes for Sound Intensity Measurements*; Report BA077-11; Brüel & Kjærum: Macquarie Park, NSW, Australia, 1987.
11. Raczyński, M. Elimination of the Phase Mismatch Error in PP Probe Using Synchronous Measurement Technique. *Pomiary Autom. Robot.* **2022**, *26*, 35–46. [CrossRef]
12. Jacobsen, F. A simple and effective correction for phase mismatch in intensity probes. *Appl. Acoust.* **1991**, *33*, 165–180. [CrossRef]
13. Yang, X.; Zhu, G.; Miao, Y. Calibration of sound intensity instruments based on the double coupler technology. *Appl. Acoust.* **2022**, *199*, 109008. [CrossRef]
14. Miao, Y.; Yang, X.; Zhu, G.; Yang, W.; Tian, J.; Dai, Y. Measurement uncertainty analysis of sound intensity using double-coupler calibration system. *Measurement* **2023**, *220*, 113315. [CrossRef]
15. Musha, T.; Taniguchi, J. Measurement of sound intensity using a single moving microphone. *Appl. Acoust.* **2005**, *66*, 579–589. [CrossRef]
16. Jacobsen, F.; Jaud, V. A note on the calibration of pressure-velocity sound intensity probes. *Acoust. Soc. Am. J.* **2006**, *120*, 830–837. [CrossRef]
17. Fernholz, C.M.; Robinson, J.H. *Fully-Coupled Fluid/Structure Vibration Analysis Using MSC/NASTRAN*; NASA Technical Memorandum 110215; National Aeronautics and Space Administration Langley Research Center: Hampton, VG, USA, 1996.
18. Marulo, F.; Beyer, T.B. NASTRAN applications for the predition of aircraft interior noise. In Proceedings of the COSMIC, 15th NASTRAN (R) Users' Colloquium, Kansas City, MO, USA, 4–8 May 1987; pp. 266–285.
19. Simcenter Nastran Acoustics User's. Available online: https://docs.plm.automation.siemens.com/data_services/resources/scnastran/2020_1/help/tdoc/en_US/pdf/acoustic.pdf (accessed on 25 July 2022).
20. NI 9234 Sound and 107 Vibration Module. Available online: https://www.ni.com/docs/en-US/bundle/ni-9234-specs/page/specs.html (accessed on 30 July 2022).
21. Bedrock. Available online: https://www.bedrock-audio.com/index.php/bedrock-talkbox-2 (accessed on 25 July 2022).
22. Walber, C.; Salzano, C.; Nowak, M.; Larratta, N. *Acoustic Methods of Microphone Calibration*; PCB Piezotronics Inc.: Depew, NY, USA, 2015.
23. BSWA Tech MP201 Free-Field Microphone. Available online: https://shop.elkome.com/en/mp201-free-field-microphone (accessed on 25 July 2022).
24. Moya, A.; Marinone, T. *Comparison of FRF Correlation Techniques*; Sandia National Laboratory (SNL-NM): Albuquerque, NM, USA, 2014.
25. Wicks, A.; Shapton, W. Frequency Response Estimators for Use in the Presence of Uncorrelated Noise. *SAE Trans.* **1987**, *96*, 62–66.